

# Metal impact and vaporization on the Moon's surface: Nano-geochemical insights into the source of lunar metals

Phillip GOPON<sup>1,2,3,\*</sup>, James O. DOUGLAS<sup>3,4</sup>, Hazel GARDNER<sup>3,5</sup>, Michael P. MOODY<sup>3</sup>, Bernard WOOD<sup>2</sup>, Alexander N. HALLIDAY<sup>2,6</sup>, and Jon WADE<sup>2</sup>

<sup>1</sup>Department of Applied Geosciences and Geophysics, University of Leoben, Leoben, Austria

<sup>2</sup>Department of Earth Science, University of Oxford, Oxford, UK

<sup>3</sup>Department of Materials, University of Oxford, Oxford, UK

<sup>4</sup>Department of Materials, Imperial College London, London, UK

<sup>5</sup>Culham Science Centre, UK Atomic Energy Authority, Abingdon, UK

<sup>6</sup>Earth Institute, Columbia University, New York, New York, USA

## \*Correspondence

Phillip Gopon, Department of Applied Geosciences and Geophysics, University of Leoben, Peter Tunner Strasse 5, Leoben 8700, Austria.

Email: [phillip.gopon@unileoben.ac.at](mailto:phillip.gopon@unileoben.ac.at)

(Received 20 June 2023; revision accepted 23 April 2024)

**Abstract**—Millimeter-to-nanometer-sized iron- and nickel-rich metals are ubiquitous on the lunar surface. The proposed origin of these metals falls into two broad classes which should have distinct geochemical signatures—(1) the reduction of iron-bearing minerals or (2) the addition of metals from meteoritic sources. The metals measured here from the Apollo 16 regolith possess low Ni (2–6 wt%) and elevated Ge (80–350 ppm) suggesting a meteoritic origin. However, the measured Ni is lower, and the Ge higher than currently known iron meteorites. In comparison to the low Ni iron meteorites, the even lower Ni and higher Ge contents exhibited by these lunar metals are best explained by impact-driven volatilization and condensation of Ni-poor meteoritic metal during their impact and addition to the lunar surface. The presence of similar, low Ni-bearing metals in Apollo return samples from geographically distant sites suggests that this geochemical signature might not be restricted to just the Apollo 16 locality and that volatility-driven modification of meteoritic metals are a common feature of lunar regolith formation. The possibility of a significant low Ni/high Ge meteoritic component in the lunar regolith, and the observation of chemical fractionation during emplacement, has implications for the interpretation of both lunar remote-sensing data and bulk geochemical data derived from sample return material. Additionally, our observation of predominantly meteoritic sourced metals has implications for the prevalence of meteoritic addition on airless planetary bodies.

## INTRODUCTION

Unlike that of the Earth, the Moon's surface is ancient, with comparatively limited geologic processes occurring after the cessation of the majority of volcanism in the Imbrian period (3.2 Ga; Hiesinger, 2006). The lunar surface, therefore, represents perhaps the best record of the space weathering processes on airless bodies, as well as the extraterrestrial material added post-formation to both

the Earth and Moon (Pieters et al., 2000; Wiesli et al., 2003). Sampled by the Apollo missions, the lunar surface is composed of a 5- to 10-m-thick regolith layer composed of unconsolidated soil, lithic fragments and boulders, a result of the brecciation of bedrock by meteoritic bombardment. Unlike the terrestrial surface, metallic iron is a common feature of the regolith samples returned by the Apollo missions (Figure 1). Based on magnetic susceptibility measurements, metallic iron (Fe<sup>0</sup>)

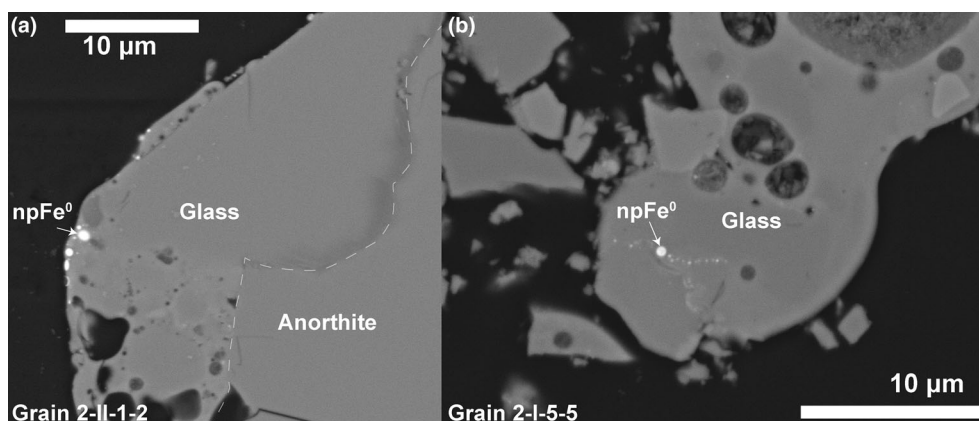


FIGURE 1. Backscattered electron images of  $\text{npFe}^0$  containing grains in sample 61501 (soil sample taken near Plum Crater). The glassy rim surrounding the anorthite grain 2-II-1-2 (a) exhibits metal aggregated toward the outer edge of the grain in contrast to (b) grain 2-I-5-5, where the  $\text{Fe}^0$  is distributed with the glassy agglutinate. Data sets R1 and R2 were acquired from the edge of grain 2-II-1-2 (Supplementary C), and data set C1 was acquired from  $\text{Fe}^0$  within the core of grain 2-I-5-5 (Supplementary C).

comprises between 0.1 and 1.8 wt% of the regolith (Cournède et al., 2012; Korotev, 1994), but the origin of these metallic components remains debated. The metallic components originate from several sources, but the relative importance of each, and their consequences for the physical, chemical, and spectral properties of the regolith remain unclear. Proposed  $\text{Fe}^0$  formation mechanisms include a combination of in situ reduction of basalt-hosted  $\text{FeO}$  and meteoritic/exogenic input and devolatilization of lunar minerals (Day, 2020; Katsura et al., 2014; Korotev, 1987; Kuhlman et al., 2015; Lucey et al., 2006; Noble et al., 2005; Wasson et al., 1975); with each having different implications for the interpretation of lunar geochemical data. The presence of an exogenic metallic meteoritic component within the regolith (estimated at 0.4%–0.5% in bulk Apollo 16 soils; Korotev, 1987) complicates the identification of the regolith's origins as well as its relationship to the wider silicate Moon. To overcome this, a variety of tracers of meteoritic addition have been used to both identify, and remove, any exogenic component from lunar geochemical data. For example, when constraining the silicate Moon's Hf/W content, the lunar sample's highly siderophile (*lit.* 'metal-loving') element (HSE) content, typically its iridium content, is measured and used to correct the data for extra-lunar input (Day et al., 2016; Kruijer et al., 2015). However, given the variable behavior of trace elements during asteroidal core formation and crystallization (Chabot & Jones, 2003; Day et al., 2016), the origin and mode of emplacement of these metallic phases, and, by extension, the assumption that they represent a chondritic HSE abundance, may introduce error. For instance, the IIAB group of iron meteorites exhibit extremely variable Ir contents (0.01–48 ppm; Wasson et al., 2007), a result of

the segregation of immiscible  $\text{FeS}$  and  $\text{FeP}$  liquids during IIAB parent body core crystallization and iridium's relative incompatibility therein (Ulff-Møller, 1998). Furthermore, emplacement into the lunar surface by high-energy impact may result in volatility induced compositional changes. Hence, assumptions of chondritic HSE abundances in lunar metals may be invalid.

The nature of regolith-hosted metallic iron is diverse, with inclusions ranging in size from tens of nanometer to a few millimeter (Goldstein, 1971; Joy et al., 2016; Morris, 1980). The smallest metallic size fraction, the so-called nanophase iron ( $\text{npFe}^0$ ), is typically considered native to the Moon and chemically distinct to the larger, micrometer scale, inclusions (Korotev, 1987; Kuhlman et al., 2015; Lucey et al., 2006). Suggested  $\text{npFe}^0$  formation mechanisms include in situ reduction of iron-bearing silicate and oxide minerals, such as ferroan anorthosite, olivine, pyroxene, and ilmenite, by either solar wind exposure (Dikov et al., 1978; Kuhlman et al., 2015; Pillinger et al., 1976), reduction by solar wind implanted hydrogen (Housley et al., 1974; Liu et al., 2012) or as a consequence of micro-meteorite bombardment (Lucey et al., 2006; Pieters et al., 2000). In contrast, the larger, ~micrometer- to millimeter-scale size fraction  $\text{Fe}^0$  is generally assumed to be either exogenic in origin and derived from the spallation of impacting iron–nickel meteorites (Gopon et al., 2017; Korotev, 1987), or native to the Moon and a result of the low oxygen fugacity prevailing during lunar basalt generation (Longhi, 1992).

Texturally, the lunar regolith's smallest size metallic fraction,  $\text{npFe}^0$ , is either found as sub-micrometer inclusions within thin rims on grains, or as inclusions within glassy agglutinates (Figure 1; Lucey et al., 2006), and typically co-located with larger metallic inclusions of

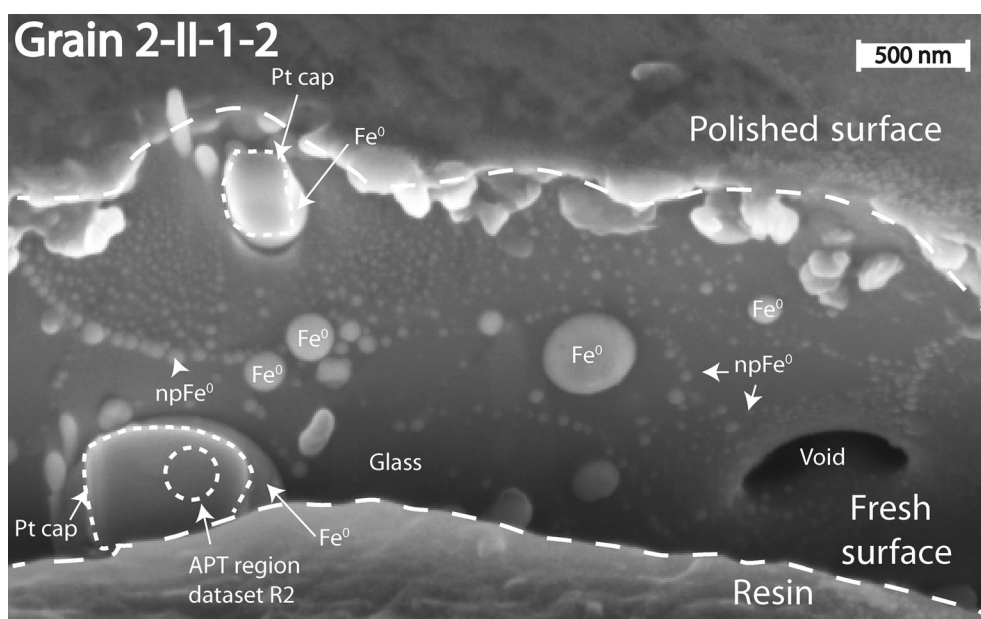


FIGURE 2. Secondary electron image of the side of a grain 2-II-1-2, showing the size diversity of  $\text{Fe}^0$  within the regolith. Shown in the bottom left is the grain that data set R2 came from, with a capping layer of protective Pt. Note this image is taken at a  $45^\circ$  stage tilt and is looking in the Z direction down the edge of the grain.

up to around 5 mm in diameter (Figure 2). Similarly, the larger micrometer- to millimeter-scale  $\text{Fe}^0$  can be found in similar textural relationships as  $\text{npFe}^0$ , with spherical and irregularly shaped metallic fragments previously noted in lunar breccias (Goldstein et al., 1972; Korotev, 1987; Misra & Taylor, 1975; Morris, 1980). Given the diverse formation mechanisms, it may be expected that regolith-hosted lunar metals exhibit a wide variability in elemental and isotopic chemistry and that the mechanisms of emplacement could also leave their mark on the metal's composition. Because of their small size, minor and trace element analyses of the sub-micrometer  $\text{npFe}^0$  have previously proven difficult. Consequently, it has not been possible to discern any continuum in composition across the different  $\text{Fe}^0$  size fractions, and hence whether the variety of sizes principally reflects differing origins. We, therefore, employed a combination of atom probe tomography (APT), low accelerating voltage ( $V_{\text{acc}}$ ) high-resolution electron probe microanalysis (HR-EPMA), and 'traditional' ('high', 15 kV $_{\text{acc}}$ ) EPMA to characterize a wide range of sizes ( $\sim 10$  nm to up to 0.5 mm) of and textural occurrences of  $\text{Fe}^0$  observed within our Apollo 16 regolith sample (61501,22). The aim of our study is to quantify the influence of in situ reduction processes versus meteoritic input, in a large size range (from a few nanometers to millimeters), of metallic components in the regolith.

The nanophase and micrometer-sized  $\text{Fe}^0$  analyzed here (170  $\text{Fe}^0$  particles  $> 5 \mu\text{m}$ ; 45 between  $\sim 1\text{--}5 \mu\text{m}$ ; and  $4 < 1 \mu\text{m}$ ) exhibit a similar range of major, minor,

and trace elemental compositions, including Fe, Ni, and Ge. The metallic Fe:Ni ratios measured here are significantly lower, and the Ge contents are significantly higher than those found in other Apollo 16 lunar minerals and rocks and more closely match meteoritic iron–nickel phases (ex: kamacite/taenite). Our modeling suggests that additional compositional modification would arise from impact related volatilization and subsequent condensation, high Ge and low ( $< 6$  wt%) Ni content iron meteorites are relatively rare and the observation that a significant portion of Fe–Ni phases in the lunar regolith have high Ge/low Ni, might have significant implications for the interpretation of the noble metal content of the silicate moon. Furthermore, the similar Ni and Ge contents of the nanometer- to micrometer-scale  $\text{Fe}^0$  suggests the same source/formation process for a significant portion of the  $\text{Fe}^0$  in the Apollo 16 regolith and, likely, in other localities.

## METHODS

### Sample Provenance and Description

Apollo 16 sample 61501,22 is a 10 g split of a "soil" sample (61500) collected from the Cayley plains along the edge of the Descartes Mountains near the Apollo 16 landing site (Ulrich et al., 1981). Sample 61500 was collected as a rake sample from the loose regolith on the rim of Flag Crater (Apollo 16 Station 1), approximately 1.5 km west of the Apollo 16 landing site, and about 1 crater diameter distance from the larger Plum Crater. It

was collected as part of a larger soil sample set that was meant to radially sample the Plum Crater ejecta (Ulrich et al., 1981). Sample 61500 has been indexed as a sub-mature soil with a  $I_s/\text{FeO} = 53$  (R. V. Morris, 1978), with a 112  $\mu\text{m}$  average grain size made up of 58% anorthosite, 35% impact melt, and 9% mare component (Butler et al., 1973; Graf, 1993; Meyer, 2010).

The lunar soil is the finest size fraction ( $<70 \mu\text{m}$ ) of the lunar regolith and represents the mixing of both locally sourced and more distal rocks ( $>120 \text{ km}$ ; Gault et al., 1974; Li & Mustard, 2005; Rhodes, 1977). As such, the regolith samples a significant portion of the regional lunar surface with limited returned sample mass.

One thousand six hundred individual dust grains from a 10 g subset of this sample (61501,22) were handpicked and mounted into four separate epoxy resin mounts (Gopon et al., 2017: Mount 1 [NASA ID: 61501,124]: 114 grains, 0.8–1 mm UV fluorescent grains; Mount 2 [NASA ID: 61501,125]: 281 grains, 0.5–0.8 mm UV fluorescent grains; Mount 3 [NASA ID: 61501,126]: 439 grains UV fluorescent grains,  $<0.5 \text{ mm}$ ; Mount 4 [NASA ID: 61501,127]: 805 grains  $<0.5 \text{ mm}$  UV/non-UV fluorescent grains). All samples in this study are identified by mount#-quadrant#-row#-grain# (e.g., 2-II-1-2 = Mount 2, quadrant II, row 1, grain 2). All 1600 grains were subsequently characterized using a scanning electron microscope (SEM) and energy-dispersive spectroscopy (EDS) to find those grains that contained  $\text{Fe}^0$  and to determine the range of textural occurrences of over which  $\text{Fe}^0$  can be found. UV, plain light, backscatter electron maps, and individual grain images are available upon request or can be found in Gopon (2016).

A random selection of  $\text{Fe}^0$  particles (219 in total; 170  $> 5 \mu\text{m}$ ; 45 between  $\sim 1$  and  $5 \mu\text{m}$ ), for a range of particle sizes (nanometer to millimeter sized), were analyzed in these grain mounts by standard (15 keV) EPMA and low voltage EPMA. Due to the time and cost associated with APT analyses, only four  $\text{Fe}^0$  particles from two representative regolith grains were analyzed. These two regolith grains represent the two textural occurrences of  $\text{Fe}^0$  that were observed in the SEM characterization of the 1600 regolith grains (within glassy agglutinates and on rims of grains; Figure 1). No other textural occurrence of nanophase  $\text{Fe}^0$  was observed in this study. Due to beam-induced damage that occurs within small particles when exposed to an electron beam for a prolonged period of time (Gopon et al., 2017), it is often problematic to analyze more than one element per spectrometer available on the EPMA; often less if the abundance of trace elements is low enough where spectrometer signals must be summed to achieve the necessary detection limits. The focus was, therefore, placed on three most diagnostic elements for our geochemical discrimination (Ni, Fe, and Ge), with multiple spectrometers summed to achieve the

necessary detection limits for our lower trace element (Ge). A larger set of elements was analyzed in the largest ( $>5 \mu\text{m}$ ) particles (additionally Co and Cu).

Previously published minor element analyses of the IIAB iron meteorites have usually employed ‘bulk’ techniques (e.g., INAA—Wasson et al., 1989, 2007), but given the presence of nickel schreibersite ( $\text{Fe}_3\text{P}$ ) enclaves, it is possible such data underrepresent the Ge content of the iron-rich phases whilst simultaneously overrepresenting their Ni contents. To test this and to compare to our Apollo 16 data, we performed a detailed EPMA study of a polished piece of the IIAB Coahuila iron meteorite (Oxford Museum of Natural History ID #: OUMNH-Mt179), with transects made toward a schreibersite enclave, representing a phosphide liquid trapped during metal core crystallization. Additionally, the silicate host grains from which the APT lift-outs were taken were analyzed, with a special emphasis placed on the ratio of Fe to Ni.

Previous attempts at determining the elemental and isotopic compositions of  $\text{npFe}^0$  contained within lunar surface material have been hindered by the spatial resolution offered by micro-analytical techniques such as laser ablation–inductively coupled plasma–mass spectrometry (LA-ICP-MS) with analytical resolutions  $\sim 10\text{--}100 \mu\text{m}$  (Wiesli et al., 2003). The inability of high-spatial resolution techniques, such as transmission electron microscopy (TEM; Thompson et al., 2016), to accurately determine minor and trace elemental abundances has further inhibited accurate measurements of chemical composition. To provide the combination of chemical and spatial resolution required to analyze lunar  $\text{npFe}^0$ , we have employed low-voltage/high-resolution electron probe microanalysis (HR-EPMA) coupled with atom probe tomography (APT) to characterize  $\text{npFe}^0$  obtained from Apollo 16 lunar regolith (sample 61501,125). While EPMA allows the identification and fully quantified elemental analyses of the larger ( $\sim 0.5$  to  $1 \mu\text{m}$ ) metallic components (Gopon et al., 2013; Hughes et al., 2018; Moy & Fournelle, 2017), APT offers the unique ability to simultaneously characterize the trace, minor, and major elements present at near atomic scale resolution, and has the potential to determine the isotopic compositions of sub-micrometer-scale phases in three dimensions (Daly et al., 2018; Gopon et al., 2017, 2020; Gopon, Douglas, et al., 2022; Gopon, Douglas, Auger, et al., 2019; Valley et al., 2014).

## EPMA Analyses

The major and trace elemental chemistry of the metal containing silicate grains was measured using a CAMECA SX-5 FE Electron Probe Microanalyzer (EPMA). Analytical conditions were 15 keV 10 nA, using a  $10\text{-}\mu\text{m}$



defocused beam to limit sample damage. Count times were 60 s on peak, with the exception of Na, which was 20 s due to the known Na mobility issue when analyzing plagioclase and glasses. Standards used were andradite (for Fe and Ca), albite (for Si, Na, and Al), sanidine (K), synthetic  $\text{TiO}_2$  (Ti), Ni metal (Ni), and synthetic MgO (Mg). One hundred and fourteen points were acquired on grain 2-II-1-2 (rim  $\text{npFe}^0$ ), and eight points were acquired on grain 2-I-5-5 (core  $\text{npFe}^0$ ). The degree of chemical heterogeneity in each sample was assessed and noted to be small. Full analyses are reported in Table A.

EPMA analyses of 170 metallic phases larger than 5  $\mu\text{m}$  were conducted at 15 keV 50 nA, with count times 240 s on peak for Ge, Cu, and Co (measured by WDS with 3 out of 5 spectrometers measuring Ge), and 60 s for P, S, Cr, Ni, and Fe (measured by EDS). Standards used were Fe metal (for Fe), Ni metal (for Ni), 99.999 purity Si wafer (for Si), Co metal (for Co), Cu metal (for Cu), Ge metal (for Ge), FeS (for S), and Durango Apatite (for Ca and P). Full analyses are reported in Table A. Approaching the phosphide (Table A), there is a similar increase in the iron's Ge content and a simultaneous decrease in Ni to ~3.5 wt%, but Ni concentrations remain above the lower range of the lunar hosted metals. Given the length scales and the association with the Ni-rich schreibersite enclave (within ~100  $\mu\text{m}$ ), the pattern observed in the Coahuila section likely represents Ni diffusion occurring after crystallization within the IIAB parent body. Similar patterns are seen in individual lunar hosted metals when associated with phosphides, again reflecting diffusion of Ni occurring on cooling.

Due to the small electron beam–sample interaction volume, low  $V_{\text{acc}}$  EPMA can result in significant beam damage arising from the reduction in electron interaction volume. Although conductive materials are not typically prone to beam damage, the insulating nature of the matrix meant that analysis time for the smaller size fraction of lunar metals (<5  $\mu\text{m}$ ) was kept to a minimum and EPMA data comprised only major element data and one trace element (Gopon, Forshaw, et al., 2022).

High-resolution EPMA (HR-EPMA) analyses of 45 individual metallic components of 61501 between ~1 and 5  $\mu\text{m}$  were conducted at 10 keV 10 nA using the protocols set out by Gopon et al. (2013, 2017) and Gopon, Forshaw, et al. (2022). Count times were 60 s on peak for Ge, Ni, and Fe (measured by WDS with 3 out of 5 spectrometers measuring Ge), and 60 s for Si, P, S, and Ca (measured by EDS). Standards used were Fe metal (for Fe), Ni metal (for Ni), 99.999 purity Si wafer (for Si), Co metal (for Co), Ge metal (for Ge), FeS (for S), and Durango Apatite (for Ca and P). Full analyses are reported in Table A. To minimize carbon buildup during analysis, the liquid nitrogen cold finger was employed.

## APT Sample Preparation

To obtain trace element data from the smallest size fraction,  $\text{npFe}^0$  was extracted for APT analyses from two representative dust grains—a glassy agglutinate and the rim of an anorthite grain. These two representative grains (2-I-5-5 and 2-II-1-2) from each of the two textural occurrences of  $\text{npFe}^0$  (on mineral rims and cores of agglutinates) that were observed were chosen from Mount 2 (NASA sample ID 61501,125). Grain 2-II-1-2 is a ~650- $\mu\text{m}$  anorthite grain containing numerous  $\text{npFe}^0$  within the grain's glassy rim (Figure 1a). Grain 2-I-5-5 is a ~40- $\mu\text{m}$  glassy agglutinate containing  $\text{npFe}^0$  within the matrix (Figure 1b).

Focused ion beam (FIB) site-specific specimen preparation lift-outs were performed using the general procedures set out by Miller et al. (2007) and the geologic specific methods in Gopon, Douglas, Wade, et al. (2019) using a Zeiss Crossbeam FIB-SEM equipped with an Oxford Instruments XmaxN 15 EDS (in the University of Oxford, David Cockayne Centre for Electron Microscopy). The lift-out geometry was chosen to maximize the number of  $\text{npFe}^0$  particles in each lift-out bar. Eleven APT needle-shaped specimens were made from slices of each of these two lift-outs. Six APT needle-shaped specimens were made from grain 2-II-1-2 (rim  $\text{npFe}^0$ ) and five from grain 2-I-5-5 (core  $\text{npFe}^0$ ). Of these specimens, three were run successfully (labeled data sets R1 and R2 from grain 2-II-1-2; and C1 from grain 2-I-5-5). Unfortunately, the remaining samples fractured during the first few minutes of APT analysis and before usable data could be obtained. This success rate (27%) is slightly lower than that reported in APT measurements (on average 40%–60% success rate; Fougereuse et al., 2023; Gopon, Douglas, Auger, et al., 2019; Peterman et al., 2016; Xie et al., 2023; etc.) of other geologic materials and is likely a result of the large differences in the electric field required to run the insulative matrix glass and the conductive iron nanoparticles.

The small size (10–1000 nm) of the  $\text{npFe}^0$  means that typical FIB milling techniques targeting  $\text{npFe}^0$  material visible on the polished surface of the grain results in the majority of the targeted feature being lost. Most of this sample destruction arises from the final polishing step, which is required to remove Ga damage imparted by the previous FIB steps. A procedure based on the work of Tang et al. (2012) was developed, which uses sequential variable voltage (2–10 keV) energy-dispersive spectroscopy (EDS) to provide chemical imaging ~0.5–1  $\mu\text{m}$  deep into the sample (Gopon, Douglas, Wade, et al., 2019). The preparation process involved initially forming the sample into a flat-sided cuboid. Using a combination of sequentially slicing ~100 nm of material

off the four sides of the sample and conducting a series of increasing voltage EDS elemental maps, we were able to find and define the extent of the  $\text{npFe}^0$  within the matrix without exposing/destroying any  $\text{npFe}^0$  (Supplementary B). Using this method, the final low-energy FIB polishing step exposed the  $\text{npFe}^0$  only at the very end of the sample preparation and maximized the volume of  $\text{npFe}^0$  available for the APT analysis.

Sequential imaging and definition of the shape of the  $\text{npFe}^0$ , without exposure to the Ga beam of the FIB-SEM, was crucial for the success of our APT analyses. In previous attempts where the variable voltage imaging method was not used, the majority (>70%) of the final APT needle-shaped specimen was composed of matrix glass (Supplementary B). This both limited the amount of  $\text{npFe}^0$  that was available for analysis in the APT specimen and increased the probability of specimen failure under the high electric field present during the APT experiment. This increased fracture probability is primarily due to the strain induced in the sample by the significant difference in evaporation field between the insulating matrix glass and conductive  $\text{npFe}^0$  (Larson et al., 1999).

## APT Experiments

APT experiments were conducted on the CAMECA LEAP 5000XR equipped with a 355 nm UV laser at the University of Oxford, Department of Materials. This instrument has a ~52% ion detection efficiency (Martin et al., 2017) and analysis conditions were as follows: stage temperature 55–60 K; 125–200 kHz pulse frequency; 40–80 pJ laser energy; detection rate of 0.003–0.005 average ions per pulse. These conditions were chosen based on previous work on similar nanophase metallic samples within the lunar regolith (Fe-Si; Gopon et al., 2017), test analyses run on lunar meteorite NWA 7986 (feldspathic vitric breccia), and a failed set of analyses run on  $\text{npFe}^0$  in grain 2-I-5-7 where all APT samples fractured. In general, higher laser energy is thought to increase sample yield, but also increases the size of thermal peak tails within the resulting mass spectra leading to a reduced signal-to-noise ratio (Gault et al., 2012). Through trial and error, the above conditions were found to achieve the best analysis success rate while maintaining reasonably small thermal peak tails.

APT data sets R1 and R2 were acquired from two separate APT needle-shaped specimens from the rim of a ~650- $\mu\text{m}$  grain of anorthite (grain 2-II-1-2; Supplementary C). Data set R1 contains 20 million ions, all of which came from a large  $\text{npFe}^0$ . Data set R2 contains 6 million ions, all of which come from a large  $\text{npFe}^0$ . The sulfur-rich regions of this data set were delineated using a 6 wt% sulfur iso-concentration surface. APT data set C1 comes from large Fe particles from the

center of a glassy agglutinate. Data set C1 contains five million ions, with ~2.5 million arising from  $\text{npFe}^0$  and the rest from the matrix glass/Pt cap. The Pt cap was placed over the  $\text{npFe}^0$  to protect it from the FIB beam during sample preparation. In C1, the top 50 nm contains gallium damage arising from the FIB preparation and/or contained within the Pt cap, so the composition of the  $\text{npFe}^0$  was determined from the 90 wt% iron iso-concentration surface below the gallium-containing zone.

## APT Data Analysis

APT data analysis was conducted using a combination of the CAMECA proprietary software (IVAS v3.8.4) and the AtomProbeLab (v0.1.4) MATLAB code (<https://sourceforge.net/projects/atomprobelab/> (London, 2019)). Reconstructions and basic image analyses were undertaken using IVAS, while all composition measurements were performed using AtomProbeLab. Ninety-five percent confidence intervals are reported and are a measure of the uncertainty in the composition, which was determined using the maximum likelihood estimation when mass spectrum peak overlaps were present. Both counting error and uncertainty from solving the peak overlaps can contribute to the overall uncertainty in composition. When no peak overlaps are present, the uncertainty is given solely by the counting error. Further details of the sources of uncertainty can be found in the work of London (2019).

Identifying peaks in the APT mass spectra was, however, challenging owing to the large number of elements and complex ions present. Several strategies and tools were employed to aid peak identification. EDS was used to obtain information on the major elements present and used as a starting point for peak identification. In addition, the custom tool ‘weights’ (Haley et al., 2015) was used to generate a list of possible species that could be contributing to a given unknown mass spectrum peak. A list of candidate ionic species was then compiled, based on the species identified as present by EDS and a manually selected subset of the list of species generated by *weights*. Many of the candidate ionic species had isotopes present at the same mass-to-charge value, resulting in mass spectrum peak overlaps. Thus, it was necessary to solve these peak overlaps to determine the most likely relative contributions to such peaks by analysis of adjacent non-overlapping isotope peaks and knowledge of their natural abundances. For each data set, deconvolution of mass spectrum peak overlaps was performed, based on the candidate ionic species that were inputted, using the method described by London (2019). The level of agreement between the heights of the peaks in the deconvolved mass spectrum and the original mass spectrum was used to aid peak identification;

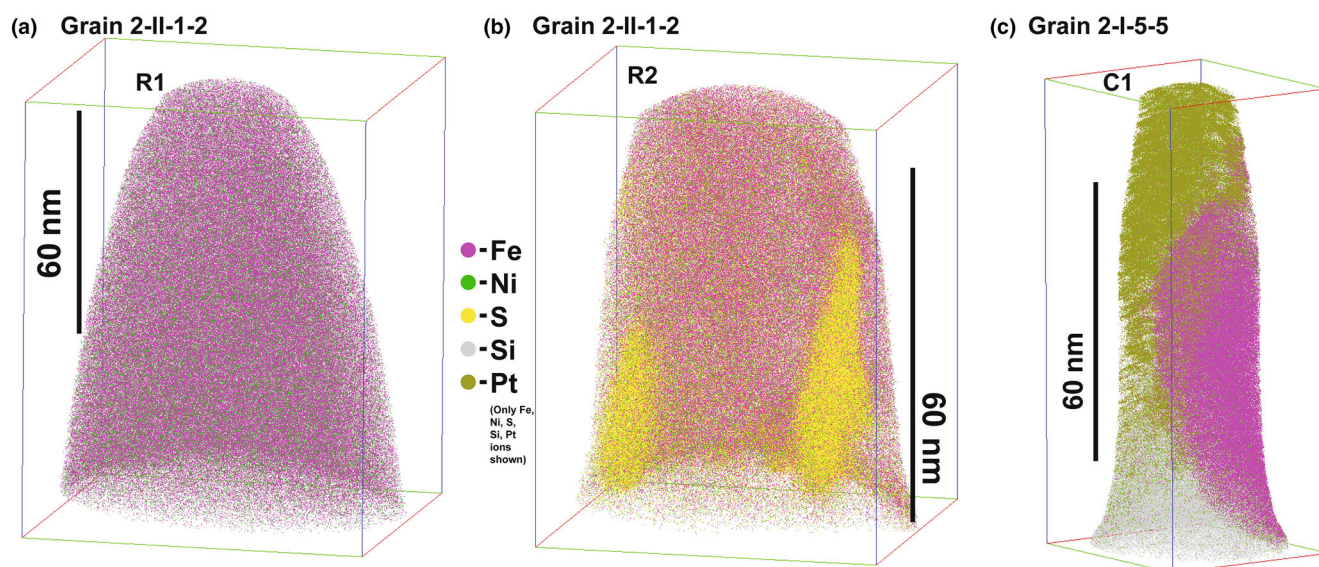


FIGURE 3. Three-dimensional volume reconstructions of the APT data sets R1 (a), R2 (b), and C1 (c). Only the Fe, Ni, S, Si, and Pt ions are shown. The Pt shown in (c) arises from the protective layer used to minimize undue sample damage during FIB extraction. Locations from which these data sets come from are noted in Supplementary C. (Color figure can be viewed at [wileyonlinelibrary.com](https://onlinelibrary.wiley.com/doi/10.1111/maps.14184))

combinations of species that led to good agreement were selected. The Akaike information criterion was also used to assist with peak identification by minimizing overfitting as described by London (2019). Despite this careful analysis, we could not identify a small number of peaks. The percentage of unidentified ions in data sets 7939, 6504, and 6622 is 1.3%, 0.05%, and 0.1%, respectively. Atom probe 3D reconstruction of the data sets can be found in Figure 3 and Supplementary D, whilst quantitative elemental analysis of the APT data sets is reported in Supplementary A. Mass spectra for each APT data set, including unidentified peaks, can be found in Supplementary E–G.

## RESULTS

Due to the inhomogeneity and the presence of conductive metal in a majority matrix of insulating silicate, the optimization of APT analysis parameters (laser fluence, repetition rate, and extraction voltage) was problematic—see APT Methods for details. Eleven atom probe specimens were prepared, with three successfully analyzed—two, labeled R1 and R2, from the rim of an anorthite grain (grain 2-II-1-2; Figures 1 and 2; Supplementary C) and one, C1 from the center of an agglutinate fragment (grain 2-I-5-5; Figure 1; Supplementary C). The approximate volumes sampled by the ‘successful’ APT data sets are given in Supplementary C. The resulting 3D APT reconstructions of these samples are shown in Figure 3, and in higher detail in Supplementary D. The accompanying mass

spectra and compositions for these data sets are reported in the Supplementary E–G. Atom probe data sets R1 and R2 were acquired from two separate APT specimens extracted from the rim of a ~650- $\mu\text{m}$  grain of anorthite (grain 2-II-1-2), and data set C1 was acquired from the core of a ~40  $\mu\text{m}$  piece of glassy agglutinate (grain 2-I-5-5).

The iron particles measured with EPMA (>1  $\mu\text{m}$ ) show a range of Fe:Ni ratios that are generally closer to Fe:Ni ratios in chondrites and iron meteorites than they are to those in mare basalts and pristine highland rocks (Figure 4; Supplementary A). APT measurements of iron particles <<1  $\mu\text{m}$  show a more limited, but broadly similar, range of Fe:Ni ratios compared to those >1  $\mu\text{m}$ . The host silicate in the grains from which APT lift-out was taken all had no Ni above our EPMA detection limits (Supplementary A). Ni and Ge concentrations within all three size fractions of iron particles (<1  $\mu\text{m}$ ; 1–5  $\mu\text{m}$ ; >5  $\mu\text{m}$ ) show similar ranges of Ge and Ni (Figure 5a). No differences in the Fe:Ni ratios or Ni versus Ge concentrations of the smallest size fraction were noted, that is, no difference was found between  $\text{npFe}^0$  in the glassy agglutinate versus the glassy rim on a ferroan anorthite grain measured with APT (Figures 4 and 5). Other geochemical tracers were investigated; however, due to the finite number of elements that could be accurately analyzed by the full range of techniques used, the emphasis was placed on precise measurements of a more limited number of only the most diagnostic geochemical tracers (i.e., Fe, Ni, Ge).



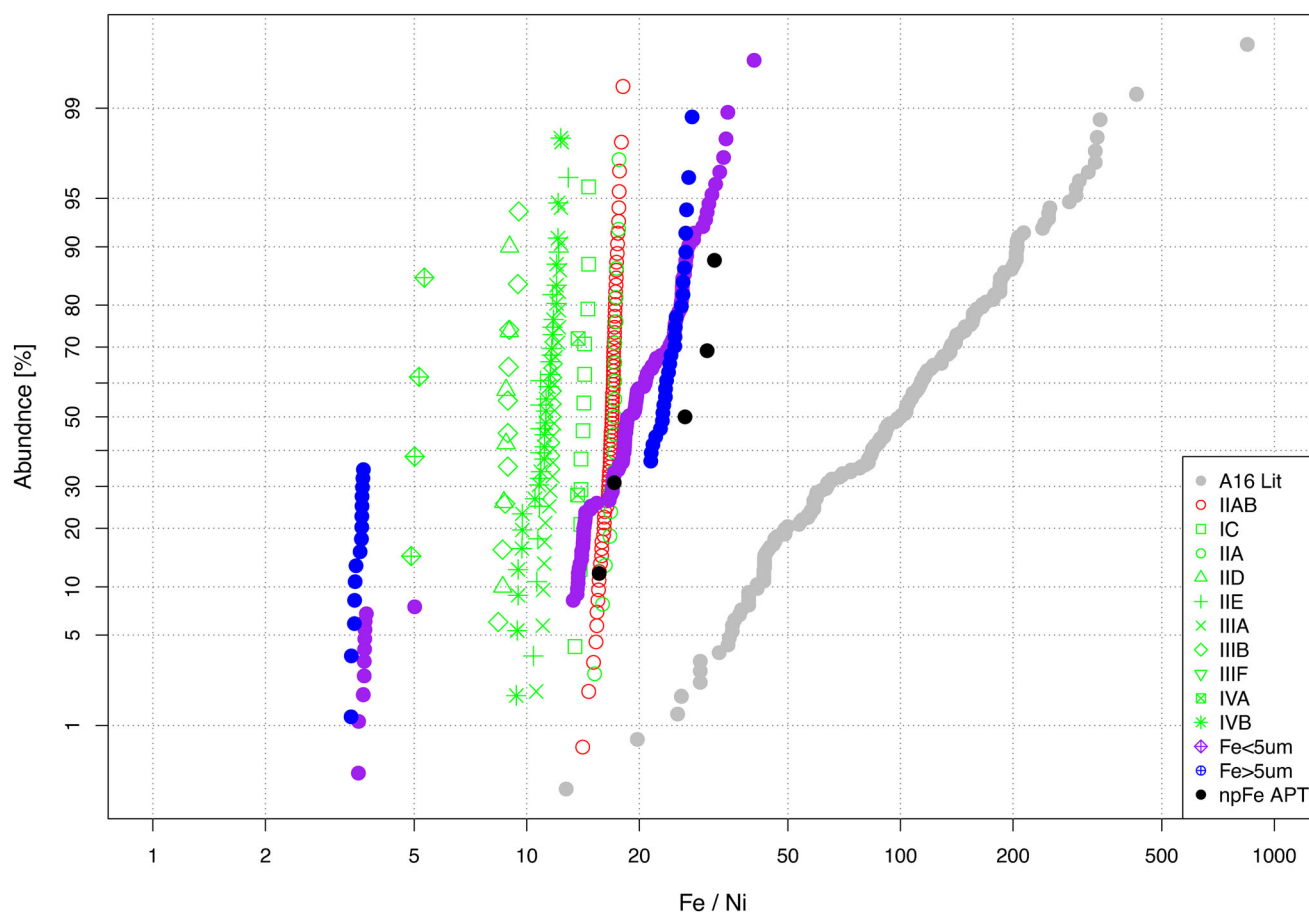


FIGURE 4. Relative abundance of a specific Fe/Ni ratio for bulk silicate analyses from other Apollo 16 samples (from the Lunar Sample Compendium (Meyer, 2010); gray), the IIAB meteorite measured here with EPMA (red), bulk geochemical measurements of iron meteorites (taken from MetBase (GeoPlatform, UG, n.d.); green), and the iron particles measured here with EPMA (purple and blue) as well as APT (black). (Color figure can be viewed at [wileyonlinelibrary.com](https://onlinelibrary.wiley.com/terms-and-conditions))

## DISCUSSION

Given the variety of likely formation mechanisms, it may be expected that metallic lunar iron will exhibit distinct geochemical signatures which signify its origins. Metal components which result from solar wind bombardment, and the subsequent in situ reduction of iron oxide, should broadly reflect the siderophile elemental composition of the silicate and oxide host, here olivine, pyroxene, ilmenite, and/or ferroan anorthosite. The low siderophile element concentrations of the mare basalts and pristine highland rocks imply that any metal produced via space weathering will also possess correspondingly low siderophile element contents (Day et al., 2016; Walker, 2009). In contrast, the chemical reduction of silicate and oxide-hosted iron which arises from meteoritic bombardment necessitates the vaporization, melting, and mixing of the impactor and target materials. Such processes would inevitably add a variable extra-lunar geochemical component (Anand et al., 2004;

Korotev, 1987; Lucey et al., 2006; R. Morris, 1978) and likely the presence of a reductant, plausibly meteoritic carbon or hydrogen arising from either solar wind implantation or contained within nominally anhydrous minerals (Gopon et al., 2017; Korotev, 1987; Kuhlman et al., 2015; Wszolek et al., 1973). Fe-Ni metal which originates solely from an extra-lunar source, exogenic iron, will principally reflect the composition of its parent body. Its emplacement into the lunar regolith may be expected to impart a compositional change, arising from melting and partial re-equilibration with Fe-bearing silicates, metals, and sulfides in soil particles and from element volatility caused by both the high temperatures of impact and the possibility of mixing with previously emplaced lunar Fe<sup>0</sup>.

Of the moderately siderophile elements measured here, Ni is significantly more refractory than Ge, whereas Fe and Ni have a similar volatility (Chabot et al., 2017; Wood et al., 2019) (50% condensation temperatures at 10<sup>-4</sup> bar, Fe 1338 K and Ni 1363 K, Wood et al., 2019). In comparison to terrestrial rocks, lunar surface rocks



exhibit significantly lower concentrations of Ni (Meyer, 2010) and as a result, the bulk silicate Moon has been inferred to be depleted by a factor of around three in Ni compared to the bulk silicate Earth (McDonough & Sun, 1995; Walter et al., 2000). The Ge content of the silicate Moon is similarly low, with the average Ge from the Apollo 16 samples being 0.59 and 0.11 ppm if breccias, glasses, and soils are excluded (Haskin & Warren, 1991; Figure 5b). Iron meteorites, however, generally contain between 6 and 10 wt% Ni with concentrations in excess of 20 wt% having been reported Ni (Figure 4) and, when compared to the silicate Moon, exhibit elevated Ge contents of 10–300 ppm (Goldstein et al., 2009; Wasson et al., 2007). The Ni and Ge contents of iron meteorites also vary by meteorite groups, reflecting both the prevailing conditions of core formation within the parent body, and post-formation processes such as the development of core liquid immiscibility (Goldstein et al., 2009). The Ni and Ge contents of metallic inclusions within lunar silicates, therefore, offer a path to discriminate between the origin of regolith hosted Fe<sup>0</sup> and, potentially, the mechanisms of their emplacement into the lunar surface. In short, the origin of metals with high Fe/Ni (>> ~100) ratios and low Ge contents (<< 100 ppm) can be proscribed to in situ reduction of lunar hosted iron. Contrastingly, high Ge contents and low Fe:Ni (<100) contents reflect an exogenic source enriched in both elements, with Ge contents further elevated by its volatility and subsequent condensation during emplacement. Importantly, given the bulk silicate Moon's low Ni and Ge contents, any mixing of an endogenic lunar iron component with metal arising from meteoritic input would serve to decrease both the Ni and Ge contents of the metals.

The smallest sized metal fraction analyzed by APT contain between 2.9 and 5.4 wt% Ni (Supplementary A; Figure 5c) and fall within the range of Ni and Ge contents of the larger, sized fraction analyzed by HR-EPMA (Supplementary A; Figure 4,5). These APT measurement are representative of the two textural occurrences of npFe<sup>0</sup> that were observed in our grain mounts (glassy rim and in the core of glassy agglutinates), and might not represent all textural occurrences possible. NpFe<sup>0</sup> on the rims of iron oxide minerals, might represent a third textural occurrence but was not observed here, likely due to their comparatively low abundances in the regolith. The Fe/Ni ratios (17.1 to 31.8) are lower than those of the surrounding host lunar silicates (Figure 4), where Ni contents are below EPMA detection limits (<~100 ppm—Supplementary A). The measured Fe/Ni ratios are also significantly below that of the average of bulk Apollo 16 samples (Figure 4; Fe/Ni ~780; Korotev, 1987). The Ni contents of the lunar metals extend to lower values than those found in iron meteorites (~6 wt%; Figure 4). This

low Ni, on its own, would suggest meteorite-sourced iron mixing with that of a low nickel iron source, that is, derived from in situ reduction of high iron silicates. However, silicates tend to not only be low in nickel but also low in germanium (BSE = 0.2 wt% Ni, 1 ppm Ge; Figure 5; McDonough & Sun, 1995). If mixing were occurring, the Ge contents of the metals should be decreasing as the nickel decreases. This mixing trend can be observed in the Apollo 16 literature data (Figure 5b); however, in the data from this study, the opposite is true (Figure 5a). In the Fe<sup>0</sup> analyzed here, the nickel concentrations go down in the metals, the Ge contents either remain constant or slightly increase (Figure 5a). The elevated Ge contents of the metals (80–350 ppm), therefore, rules out dilution of meteoritic metal with silicates.

This observation, surprisingly, suggests an entirely meteoritic origin for these lunar metals, but one which calls for a mechanism to extend the range of Ni contents to yet lower concentrations while maintaining or increasing Ge values.

Iron meteorites represent the cores of asteroidal bodies that underwent metal–silicate differentiation under low-pressure conditions, with the Ni contents of their cores primarily controlled by the redox conditions for core–mantle segregation (Frost & McCammon, 2008), with influence from fractional crystallization (Goldstein et al., 2009; Figure 5c). Nickel is notably more siderophile than iron (Chabot et al., 2005). Therefore, if a chondritic Ni content is incorporated into the asteroidal core, as would occur in a small body undergoing core–mantle differentiation under reducing conditions, then core contents of ~6 wt% Ni are expected. Metallic core Ni contents in excess of ~6 wt% hence reflect asteroidal core formation occurring under conditions more oxidizing than that witnessed by the Earth, resulting in smaller metallic cores exhibiting elevated Ni contents (Rubin, 2018). Six weight percent nickel is then the lowest amount that can be reasonably derived purely from metal–silicate differentiation and subsequent core crystallization occurring in small chondritic parent bodies (Figure 5c).

Of the iron meteorites, the IIAB, IIG, and IC exhibit broadly similar ranges of Ni and Ge mass fractions reported in this study (Figure 5c) (Buchwald, 1975). Of those, the IIABs exhibit the lowest Ni concentrations (between 5 and 6 wt%), as well as similarly elevated Ge contents to our new data (>130 ppm; Goldstein et al., 2009; Malvin et al., 1984). This is a consequence of the elevated S and P contents in the IIAB parent body core, which elevate Ge and lower Ni when core crystallization proceeds close to, or in, the two liquid (Fe–P and Fe–S) immiscibility field. Under these conditions, Ni is less compatible in the crystallizing iron solid than Ge, especially when the residual liquid has crossed the FeP–

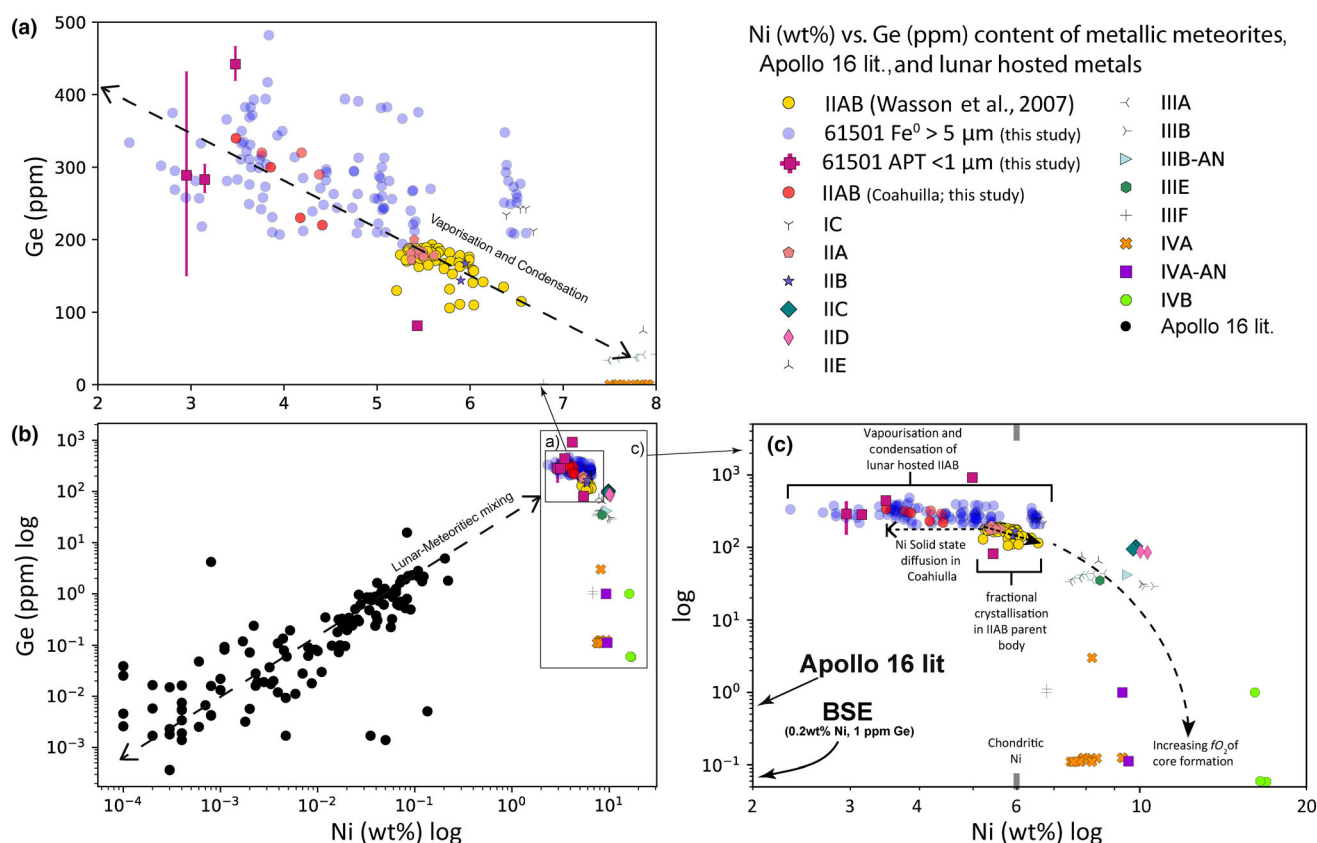


FIGURE 5. Nickel versus Germanium plots of the iron meteorites presenting various portions of the data to illustrate different trends: (a) linear/linear covering only the range of Fe<sup>0</sup> in this study highlighting the increase in Ge versus Ni; (b) log/log showing the entire range of data highlighting how far away the Apollo 16 lit. values lie from our data as well as the mixing line in the Apollo data between a wholly lunar (low Ge/low Ni) and a meteoritic (high Ge/high Ni) origin; (c) log/log showing only the range of Fe<sup>0</sup> in this study and metallic meteorites. Above 6 wt% Ni, the iron meteorites exhibit a decrease in Ge contents with increasing Ni contents, a consequence of increasingly smaller parent body cores as the oxygen fugacity ( $fO_2$ ) of core formation increases. IIABs, however, exhibit the converse relationship with, typically, increasing Ge as Ni contents decrease from ~6 to 5 wt% Ni, a result of parent body core crystallization occurring in the two liquid (Fe-S and Fe-P) immiscibility fields. HR-EPMA and ATP analysis of lunar-hosted Fe<sup>0</sup> extends this trend to Ni contents ~2 wt% and Ge contents of up to 350 ppm, reflecting the volatile behavior of Ge and, compared to Fe, the more refractory behavior of Ni during high-temperature impact and emplacement. Data are taken from MetBase (GeoPlatform, UG, n.d.), IIAB meteorites from Wasson et al. (2007), Lunar Sample Compendium (Meyer, 2010), and this study. (Color figure can be viewed at [wileyonlinelibrary.com](https://onlinelibrary.wiley.com/terms-and-conditions))

FeS liquid immiscibility boundary (Chabot et al., 2017). Nickel contents in the range 5–6 wt% hence represent the slow cooling of IIAB, or similar, parent body (Wasson et al., 2007) and the segregation of two immiscible sulfur and phosphorus-rich liquids (Ulff-Møller, 1998) above a crystallizing metallic inner core. The solid–liquid partitioning behavior of Ni and Ge results in the crystallizing metal exhibiting progressively lower Ni contents and simultaneously higher Ge contents (Chabot et al., 2017; Chabot & Drake, 2000).

The range of Ni and Ge contents exhibited by lunar metals extends this trend to Ni concentrations as low as ~2 wt% and simultaneously higher Ge contents, which cannot be explained by further cooling in a parent body alone. The observed anticorrelation between Ni and Ge in

the iron-rich metals (Figure 5a,c) is most reasonably explained by the relative volatilities of Fe, Ge, and Ni. Using thermodynamic data for the pure elements contained within (Barin et al., 1989), and assuming a representative lunar atmospheric pressure of 0.3 nPa, we may calculate the approximate composition of the gas phase that would be generated by partial vaporization of the metallic core of a body with type IIAB composition (Wasson et al., 2007). If such a core of composition 95% Fe, 5% Ni, and trace Ge were partially vaporized at 2000 K, the gas phase would be approximately 97.5% Fe and 2.5% Ni, with strong enrichment in Ge relative to the starting material (Figure 6). Re-condensation of the gas would begin with Ni enrichment and Ge impoverishment relative to the bulk gas composition and continue with

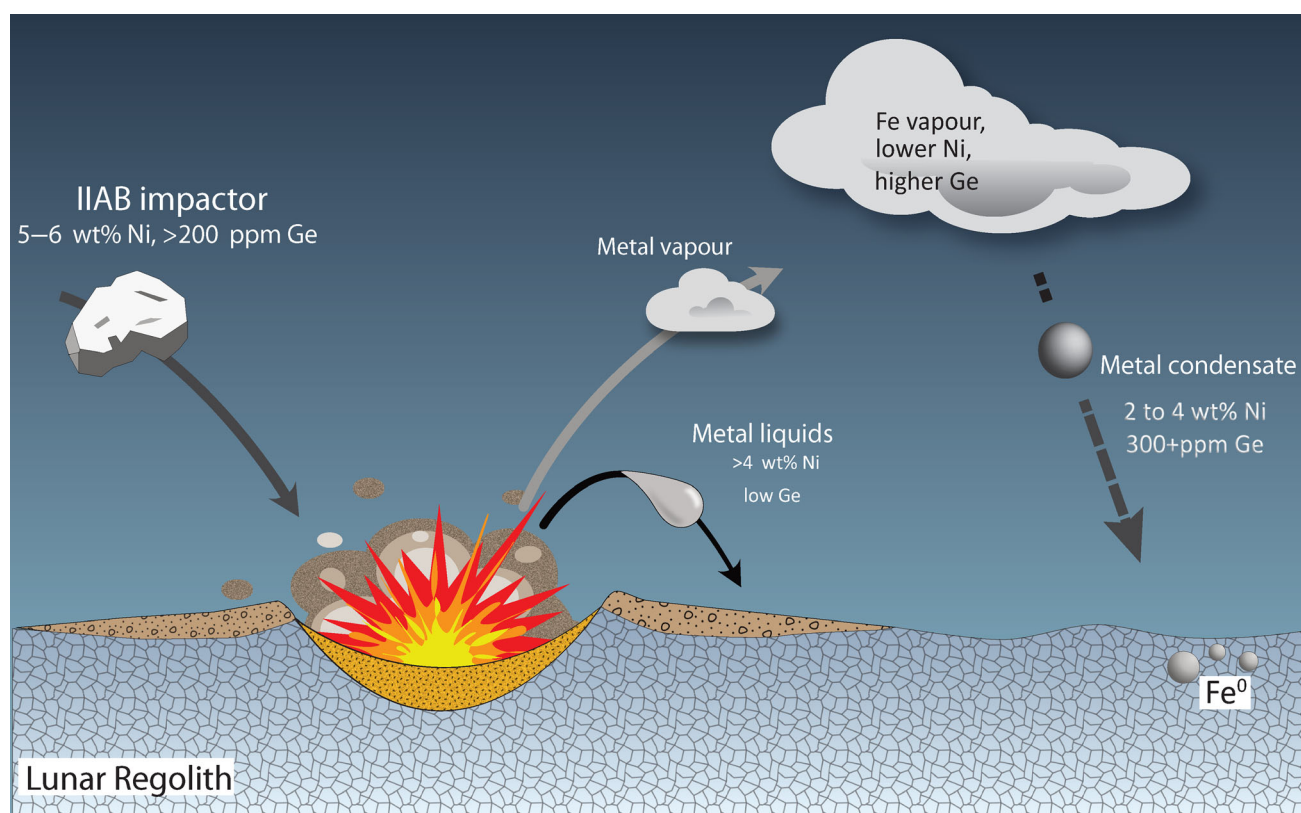


FIGURE 6. Cooling and crystallization of the IIAB parent body core occurs close to, or in, the two liquid (Fe-P and Fe-S) immiscibility field (Ulff-Møller, 1998; Wasson et al., 2007), such that the IIABs exhibit Ni contents in the 5 to 6 wt% Ni range and Ge contents greater than that seen in the other iron meteorites. The high temperatures of impact results in a metal vapor and a subsequent condensate which, in comparison to the liquid metal phase, is enriched in Fe and Ge and depleted in the more refractory Ni. The complementary liquid metal should possess elevated Ni contents and correspondingly lower Ge. However, these metals remain unidentified in the regolith given the similarity of Ni and Ge to other iron meteorites and the lack of ancillary trace element data required to make a positive identification. (Color figure can be viewed at [wileyonlinelibrary.com](https://onlinelibrary.wiley.com/terms-and-conditions))

declining Ni and increasing Ge concentrations. If vaporization took place at a higher temperature of 3000 K, close to the boiling point of Fe at 1 atm pressure, the fractionations would be lower, but the sense would be the same. For vaporization of a liquid of 95% Fe and 5% Ni, the gas would be 96.1% Fe and 3.9% Ni with Ge enrichment in the gas relative to the liquid, as before. Re-condensation would take place with the same anticorrelation of Ni to Ge as before but would be shifted to higher average concentration of Ni and lower Ge (Figure 6).

Low Ni, high Ge-bearing metals also appear in the Apollo 16 regolith, and similar metallic components with Ni contents of 2–5 wt% have been recorded in a number of other Apollo mission return samples (El Goresy et al., 1971; Papike et al., 1991; Reid et al., 1970; Seddio et al., 2014). Although the abundance of IIABs, IIGs, and ICs iron meteorites in the records is relatively low (Rubin, 2018), the widespread distribution of the metals with a geochemical signature similar to them (i.e., Ni 2%–

6%) attests to volatility-driven processes being prevalent during meteorite addition to the Moon. Unfortunately, the literature relating to lunar Fe<sup>0</sup> data contains few analyses of the trace elements required to better constrain the source of the iron. However, with the general trend in our representative data to lower Ni and higher Ge, it is reasonable to infer similar Ge contents for the lunar Fe<sup>0</sup> that exhibit similarly low Ni values.

Of course, it is possible that these meteorite-derived metals originated from multiple iron meteorite impacts across the lunar surface. However, the relative rarity of low Ni/high Ge iron meteorites (Hutchison, 1975) would argue against such a high flux of such a rare meteorite. It seems possible, therefore, that a single large meteorite and its subsequent breakup during impact may be responsible for the strange Ni and Ge signals we note across the lunar surface. Unfortunately, the paucity of trace element data of both bulk regolith and the metallic phases it contains, particularly that of the high siderophile elements, prevents firm conclusions as to the origins of lunar-hosted iron.



Further analyses of the regolith-hosted Fe<sup>0</sup> obtained from areas surrounding any of the large impact basins (i.e., Aitken Basin, Imbrium Basin, Tranquillitatis Basin, etc.) would be particularly welcoming and may enable tighter constraints to be placed on the origins, and consequences, of these significant impact events.

## CONCLUSIONS

- Micrometer to atomic scale measurements of Fe<sup>0</sup> particles within Apollo 16 regolith (sample 61501) show a similar range of major and trace elemental concentrations. This implies that the larger Fe<sup>0</sup> and nanophase Fe<sup>0</sup> have a similar formation mechanism.
- Of the two proposed formation mechanisms of Fe<sup>0</sup> in the lunar regolith (in situ reduction vs. addition of meteoritic material), our geochemical tracers of Fe, Ni, and Ge more closely match a meteoritic input than in situ reduction. Of the various meteorite groups, our data most closely match those of the iron meteorite family, and more specifically the IIAB group.
- In some of the Fe<sup>0</sup>, the Ni concentrations extend lower, and the Ge concentrations extend higher, compared to those reported in the meteorite literature. This suggests a spallation and re-condensation process of meteoritic material, which would have the effect of enriching the Ge and decreasing the Ni of the condensates.
- Similar Ni and Fe concentrations to those reported here have been reported across the Apollo landing sites. This might indicate a widespread addition of meteoritic material from the relatively rare IIAB iron (or related) meteorite group.

**Acknowledgments**—This study was supported by the Oxford Department of Materials, EPSRC Strategic Equipment Fund (grants EP/N010868/ and EP/M022803/1), Wisconsin Space Grant Consortium, NASA (NNH07ZDA001N-LASER), NSF (EAR13-37156), Lunar Sample Request Number (#2927; #3057), and the University of Wisconsin–Madison. The authors would also like to thank Ryan Zeigler, John Valley, Thomas Kelly, Stella Pedrazzini, and the entire Research group in Atom Probe TOMography and Reconstruction at the Oxford Department of Materials (RAPTOR).

**Editorial Handling**—Dr. A. J. Timothy Jull

## REFERENCES

- Anand, M., Taylor, L. A., Nazarov, M. A., Shu, J., Mao, H.-K., and Hemley, R. J. 2004. Space Weathering on Airless Planetary Bodies: Clues from the Lunar Mineral Hapkeite. *Proceedings of the National Academy of Sciences of the United States of America* 101: 6847–51. <https://doi.org/10.1073/pnas.0401565101>.
- Barin, I., Sauer, F., Schultze-Rhonhof, E., and Shend, W. S. 1989. *Thermochemical Data of Pure Substances, Part I and Part II*. Weinheim, Germany: VCH Verlagsgesellschaft mbH.
- Buchwald, V. F. 1975. *Handbook of Iron Meteorites: Handbook of Iron Meteorites*. Tempe, AZ: Arizona State University.
- Butler, J. C., Greene, G. M., and King, E. A. 1973. Grain Size Frequency Distribution and Modal Analysis of Apollo 16 Fines. *4th Lunar and Planetary Science Conference*, pp. 267–278.
- Chabot, N. L., and Drake, M. J. 2000. Crystallization of Magmatic Iron Meteorites: The Effects of Phosphorus and Liquid Immiscibility. *Meteoritics & Planetary Science* 35: 807–816. <https://doi.org/10.1111/j.1945-5100.2000.tb01464.x>.
- Chabot, N. L., Draper, D. S., and Agee, C. B. 2005. Conditions of Core Formation in the Earth: Constraints from Nickel and Cobalt Partitioning. *Geochimica et Cosmochimica Acta* 69: 2141–51. <https://doi.org/10.1016/j.gca.2004.10.019>.
- Chabot, N. L., and Jones, J. H. 2003. The Parameterization of Solid Metal-Liquid Metal Partitioning of Siderophile Elements. *Meteoritics & Planetary Science* 38: 1425–36.
- Chabot, N. L., Wollack, E. A., McDonough, W. F., Ash, R. D., and Saslow, S. A. 2017. Experimental Determination of Partitioning in the Fe-Ni System for Applications to Modeling Meteoritic Metals. *Meteoritics & Planetary Science* 52: 1133–45. <https://doi.org/10.1111/maps.12864>.
- Cournède, C., Gattacceca, J., Rochette, P., Cournède, C., Gattacceca, J., and Rochette, P. 2012. Magnetic Study of Large Apollo Samples: Possible Evidence for an Ancient Centered Dipolar Field on the Moon. *Earth and Planetary Science Letters* 331: 31–42. <https://doi.org/10.1016/j.epsl.2012.03.004>.
- Daly, L., Bland, P. A., Tessalina, S., Saxey, D. W., Reddy, S. M., Fougereuse, D., Rickard, W. D. A., et al. 2018. Defining the Potential of Nanoscale Re-Os Isotope Systematics Using Atom Probe Microscopy. *Geostandards and Geoanalytical Research* 42: 279–299. <https://doi.org/10.1111/ggr.12216>.
- Day, J. M. D. 2020. Metal Grains in Lunar Rocks as Indicators of Igneous and Impact Processes. *Meteoritics & Planetary Science* 15: 13544. <https://doi.org/10.1111/maps.13544>.
- Day, J. M. D., Brandon, A. D., and Walker, R. J. 2016. Highly Siderophile Elements in Earth, Mars, the Moon, and Asteroids: Highly Siderophile and Strongly Chalcophile Elements in High-Temperature. *Geochemistry and Cosmochemistry* 81: 161–238. <https://doi.org/10.2138/rmg.2016.81.04>.
- Dikov, Y. P., Bogatkov, O. A., Barsukov, V. L., Floresny, K. P., Ivanov, A. V., Nemeshkalenko, V. V., Alyoshin, V. G., and Chudinov, M. G. 1978. Some Features of the Main Element Conditions in Surface Layers of the Regolith Particles of the Luna Automatic Stations Samples: X-Ray Photoelectronic Spectroscopy Studies. *9th Lunar and Planetary Science Conference*, pp. 2111–24.
- El Goresy, A., Ramdohr, P., and Taylor, L. A. 1971. The Opaque Minerals in the Lunar Rocks from Oceanus Procellarum. *2nd Lunar Science Conference* 1: 219–235.

- Fougerouse, D., Cugerone, A., Reddy, S. M., Luo, K., and Motto-Ros, V. 2023. Nanoscale Distribution of Ge in Cu-Rich Sphalerite. *Geochimica et Cosmochimica Acta* 346: 223–230. <https://doi.org/10.1016/j.gca.2023.02.011>.
- Frost, D. J., and McCammon, C. A. 2008. The Redox State of Earth's Mantle. *Annual Review of Earth and Planetary Sciences* 36: 389–420. <https://doi.org/10.1146/annurev.earth.36.031207.124322>.
- Gault, B., Moody, M. P., Cairney, J. M., and Ringer, S. P., 2012. *Atom Probe Microscopy*, edited by Z. M. Hull, R. Jagadish, C. Osgood, R. M. Parisi, Jr., and J. Wang, vol. 1, 411. New York, NY: Springer. <https://doi.org/10.1017/CBO9781107415324.004>.
- Gault, D. E., Hörz, F., Brownlee, D. E., and Hartung, J. 1974. Mixing of the Lunar Regolith. *5th Lunar Conference* 3: 2365–86.
- GeoPlatform UG. n.d. Metbase: Meteorite Information.
- Goldstein, J. I. 1971. Metallic Inclusions and Metal Particles in the Apollo 12 Lunar Soil. *2nd Lunar Science Conference* 1: 177–191.
- Goldstein, J. I., Axon, H. J., and Yen, C. F. 1972. Metallic Particles in the Apollo 14 Lunar Soil. *3rd Lunar Science Conference* 1: 1037–64.
- Goldstein, J. I., Scott, E. R. D., and Chabot, N. L. 2009. Iron Meteorites: Crystallization, Thermal History, Parent Bodies, and Origin. *Chemie der Erde* 69: 293–325. <https://doi.org/10.1016/j.chemer.2009.01.002>.
- Gopon, P. 2016. *Electron Probe Sub-Micron Analysis in Geoscience: Problems and Potential Solutions of Low Voltage Electron Microprobe Analysis, as Applied to Reduced Lunar Phases and Pyroxene Lamellae*, 192. Madison, WI: University of Wisconsin.
- Gopon, P., Douglas, J. O., Auger, M. A., Hansen, L., Wade, J., Cline, J. S., Robb, L. J., and Moody, M. P. 2019. A Nanoscale Investigation of Carlin-Type Gold Deposits: An Atom-Scale Elemental and Isotopic Perspective. *Economic Geology* 114: 1123–33. <https://doi.org/10.5382/econgeo.4676>.
- Gopon, P., Douglas, J. O., Meisenkothen, F., Singh, J., London, A. J., and Moody, M. P. 2022. Atom Probe Tomography for Isotopic Analysis: Development of the S/S System in Sulfides. *Microscopy and Microanalysis* 28: 1127–40. <https://doi.org/10.1017/S1431927621013568>.
- Gopon, P., Douglas, J. O., Wade, J., and Moody, M. P. 2019. Complementary SEM-EDS/FIB-SEM Sample Preparation Techniques for Atom Probe Tomography of Nanophase-Fe<sup>0</sup> in Apollo 16 Regolith Sample 61501,22. *Microscopy and Microanalysis* 25: 2544–45. <https://doi.org/10.1017/s143192761901345x>.
- Gopon, P., Forshaw, J. B., Wade, J., Waters, D. J., Gopon, C., and Bay, S. 2022. Seeing through Metamorphic Overprints in Archean Granulites: Combined High Resolution Thermometry and Phase Equilibrium Modeling of the Lewisian Complex, Scotland. *American Mineralogist* 107: 1487–1500. <https://doi.org/10.2138/am-2022-8214ccby>.
- Gopon, P., Fournelle, J., Sobol, P. E., and Llovet, X. 2013. Low-Voltage Electron-Probe Microanalysis of Fe–Si Compounds Using Soft X-Rays. *Microscopy and Microanalysis* 19: 1698–1708. <https://doi.org/10.1017/S1431927613012695>.
- Gopon, P., Singh, J., London, A., Hansen, L., Wade, J., and Moody, M. 2020. Extraction of S Isotopes from Geologic Datasets. *Proceedings of the Field Emission Society Special APT Software Meeting*: 1. [https://youtu.be/CqI8\\_aurYrw](https://youtu.be/CqI8_aurYrw).
- Gopon, P., Spicuzza, M. J., Kelly, T. F., Reinhard, D., Prosa, T. J., and Fournelle, J. 2017. Ultra-Reduced Phases in Apollo 16 Regolith: Combined Field Emission Electron Probe Microanalysis and Atom Probe Tomography of Submicron Fe-Si Grains in Apollo 16 Sample 61500. *Meteoritics & Planetary Science* 22: 1–22. <https://doi.org/10.1111/maps.12899>.
- Graf, J. C. 1993. Lunar Soils Grain Size Catalog. *NASA Reference Publication* 1265: 1–508.
- Haley, D., Choi, P., and Raabe, D. 2015. Guided Mass Spectrum Labelling in Atom Probe Tomography. *Ultramicroscopy* 159: 338–345. <https://doi.org/10.1016/j.ultramic.2015.03.005>.
- Haskin, L., and Warren, P. 1991. Lunar Chemistry. In *Lunar Sourcebook: A User's Guide to the Moon*, 357–474. New York, NY: Cambridge University Press.
- Hiesinger, H. 2006. New Views of Lunar Geoscience: An Introduction and Overview. *Reviews in Mineralogy and Geochemistry* 60: 1–81. <https://doi.org/10.2138/rmg.2006.60.1>.
- Housley, R. M., Cirlin, E. H., Paton, N. E., and Goldberg, I. B. 1974. Solar Wind and Micrometeorite Alteration of the Lunar Regolith. *5th Lunar Conference* 3: 2623–42.
- Hughes, E. C., Buse, B., Kearns, S. L., Blundy, J. D., Kilgour, G., Mader, H. M., Brooker, R. A., et al. 2018. High Spatial Resolution Analysis of the Iron Oxidation State in Silicate Glasses Using the Electron Probe. *American Mineralogist* 103: 1473–86. <https://doi.org/10.2138/am-2018-6546CCBY>.
- Hutchison, R. 1975. Iron Meteorite Classification. In *Handbook of Iron Meteorites*, 143. Berkeley, CA: University of California Press. <https://doi.org/10.1038/265768a0>.
- Joy, K. H., Crawford, I. A., Curran, N. M., Zolensky, M., Fagan, A. F., and Kring, D. A. 2016. The Moon: An Archive of Small Body Migration in the Solar System. *Earth, Moon and Planets* 118: 133–158. <https://doi.org/10.1007/s11038-016-9495-0>.
- Katsura, T., Nakamura, A. M., Takabe, A., Okamoto, T., Sangen, K., Hasegawa, S., Liu, X., and Mashimo, T. 2014. Laboratory Experiments on the Impact Disruption of Iron Meteorites at Temperature of Near-Earth Space. *Icarus* 241: 1–12. <https://doi.org/10.1016/j.icarus.2014.06.007>.
- Korotev, R. L. 1987. The Nature of the Meteoritic Components of Apollo 16 Soil, as Inferred from Correlations of Iron, Cobalt, Iridium, and Gold with Nickel. *Journal of Geophysical Research* 92: E447. <https://doi.org/10.1029/JB092iB04p0E447>.
- Korotev, R. L. 1994. Compositional Variation in Apollo 16 Impact-Melt Breccias and Inferences for the Geology and Bombardment History of the Central Highlands of the Moon. *Geochimica et Cosmochimica Acta* 58: 3931–69. [https://doi.org/10.1016/0016-7037\(94\)90372-7](https://doi.org/10.1016/0016-7037(94)90372-7).
- Kruijer, T. S., Kleine, T., Fischer-Gödde, M., and Sprung, P. 2015. Lunar Tungsten Isotopic Evidence for the Late Veneer. *Nature* 520: 534–37. <https://doi.org/10.1038/nature14360>.
- Kuhlman, K. R., Sridharan, K., and Kvit, A. 2015. Simulation of Solar Wind Space Weathering in Orthopyroxene. *Planetary and Space Science* 115: 1–5. <https://doi.org/10.1016/j.pss.2015.04.003>.
- Larson, D. J., Prosa, T. J., Ulfig, R. M., Geiser, B. P., and Kelly, T. F. 1999. *Local Electrode Atom Probe Tomography: A User's Guide*, 328. New York: Springer. <https://doi.org/10.1007/978-1-4614-8721-0>.

- Li, L., and Mustard, J. F. 2005. On Lateral Mixing Efficiency of Lunar Regolith. *Journal of Geophysical Research E: Planets* 110: 1–16. <https://doi.org/10.1029/2004JE002295>.
- Liu, Y., Guan, Y., Zhang, Y., Rossman, G. R., Eiler, J. M., and Taylor, L. A. 2012. Direct Measurement of Hydroxyl in the Lunar Regolith and the Origin of Lunar Surface Water. *Nature Geoscience* 5: 779–782. <https://doi.org/10.1038/ngeo1601>.
- London, A. J. 2019. Quantifying Uncertainty from Mass-Peak Overlaps in Atom Probe Microscopy. *Microscopy and Microanalysis* 25: 378–388. <https://doi.org/10.1017/S1431927618016276>.
- Longhi, J. 1992. Experimental Petrology and Petrogenesis of Mare Volcanics. *Geochimica et Cosmochimica Acta* 56: 2235–51.
- Lucey, P., Korotev, R. L., Gillis, J. J., Taylor, L. A., Lawrence, D., Campbell, B. A., Elphic, R., et al. 2006. Understanding the Lunar Surface and Space-Moon Interactions. *Reviews in Mineralogy and Geochemistry* 60: 83–219. <https://doi.org/10.2138/rmg.2006.60.2>.
- Malvin, D. J., Wang, D., and Wasson, J. T. 1984. Chemical Classification of Iron Meteorites-X. Multielement Studies of 43 Irons, Resolution of Group IIIIE from IIIAB, and Evaluation of Cu as a Taxonomic Parameter. *Geochimica et Cosmochimica Acta* 48: 785–804. [https://doi.org/10.1016/0016-7037\(84\)90101-7](https://doi.org/10.1016/0016-7037(84)90101-7).
- Martin, T., London, A., Jenkins, B., Hopkins, S., Douglas, J., Styman, P., Bagot, P., and Moody, M. P. 2017. Comparing the Consistency of Atom Probe Tomography Measurements of Small-Scale Segregation and Clustering between the LEAP 3000 and LEAP 5000 Instruments. *Microscopy and Microanalysis* 23: 227–247.
- McDonough, W. F., and Sun, S.-s. 1995. The Composition of the Earth. *Chemical Geology* 120: 223–253.
- Meyer, C. 2010. Lunar Sample Compendium. *41st Lunar and Planetary Science Conference*, p. 1016.
- Miller, M. K., Russell, K. F., Thompson, K., Alvis, R., and Larson, D. J. 2007. Review of Atom Probe FIB-Based Specimen Preparation Methods. *Microscopy and Microanalysis* 13: 428–436.
- Misra, K. C., and Taylor, L. A. 1975. Characteristics of Metal Particles in Apollo 16 Rocks. *6th Lunar Science Conference* 1: 615–639. <https://doi.org/10.16309/j.cnki.issn.1007-1776.2003.03.004>.
- Morris, R. 1978. In Situ Reworking (Gardening) of the Lunar Surface: Evidence from the Apollo Cores. *9th Lunar and Planetary Science Conference Proceedings* 9: 1801–11. <http://adsabs.harvard.edu/full/1978LPSC....9.1801M>.
- Morris, R. V. 1978. The Surface Exposure (Maturity) of Lunar Soils: Some Concepts and Is/FeO Compilation. *9th Lunar and Planetary Science Conference*, pp. 2287–97.
- Morris, R. V. 1980. Origins and Size Distribution of Metallic Iron Particles in the Lunar Regolith. *11th Lunar and Planetary Science Conference* 11: 1697–1712.
- Moy, A., and Fournelle, J. 2017. Quantitative Electron Probe Microanalysis of Fe at Low Accelerating Voltage Using the  $L\alpha$  and  $L\beta$  X-Ray Lines. *Microscopy and Microanalysis* 23: 1058–59. <https://doi.org/10.1017/S1431927617005955>.
- Noble, S. K., Keller, L. P., and Pieters, C. M. 2005. Evidence of Space Weathering in Regolith Breccias I: Lunar Regolith Breccias. *Meteoritics & Planetary Science* 40: 397–408. <https://doi.org/10.1111/j.1945-5100.2005.tb00390.x>.
- Papike, J., Taylor, L., and Simon, S. 1991. *Lunar Minerals*, 121–181. New York, NY: Cambridge University Press.
- Peterman, E. M., Reddy, S. M., Saxey, D. W., Snoeyenbos, D. R., Rickard, W. D. A., Fougereuse, D., and Kylander-clark, A. R. C. 2016. Nanogeochronology of Discordant Zircon Measured by Atom Probe Microscopy of Pb-Enriched Dislocation Loops. *Science Advances* 2: 1–9. <https://doi.org/10.1126/sciadv.1601318>.
- Pieters, C. M., Taylor, L. A., Noble, S. K., Keller, L. P., Hapke, B. W., Morris, R. V., Allen, C. C., McKay, D. S., and Wentworth, S. J. 2000. Space Weathering on Airless Bodies: Resolving a Mystery with Lunar Samples. *Meteoritics & Planetary Science* 35: 1101–7. <https://doi.org/10.1111/j.1945-5100.2000.tb01496.x>.
- Pillinger, C. T., Gardiner, L. R., and Jull, A. J. 1976. Preferential Sputtering as a Method of Producing Metallic Iron, Inducing Major Element Fractionation and Trace Element Enrichment. *Earth and Planetary Science Letters* 33: 289–299.
- Reid, A. M., Meyer, C., Harmon, R. S., and Brett, R. 1970. Metal Grains in Apollo 12 Igneous Rocks. *Earth and Planetary Science Letters* 9: 1–5.
- Rhodes, J. M. 1977. Some Compositional Aspects of Lunar Regolith Evolution: Philosophical Transactions of the Royal Society A: Mathematical, Physical and Engineering Sciences 285: 293–301. <https://doi.org/10.1098/rsta.1977.0068>.
- Rubin, A. E. 2018. Carbonaceous and Noncarbonaceous Iron Meteorites: Differences in Chemical, Physical, and Collective Properties. *Meteoritics & Planetary Science* 53: 2357–71. <https://doi.org/10.1111/maps.13128>.
- Seddio, S. M., Jolliff, B. L., Korotev, R. L., and Carpenter, P. K. 2014. Thorite in an Apollo 12 Granite Fragment and Age Determination Using the Electron Microprobe. *Geochimica et Cosmochimica Acta* 135: 307–320. <https://doi.org/10.1016/j.gca.2014.03.020>.
- Tang, F., Gianola, D. S., Moody, M. P., Hemker, K. J., and Cairney, J. M. 2012. Observations of Grain Boundary Impurities in Nanocrystalline Al and their Influence on Microstructural Stability and Mechanical Behaviour. *Acta Materialia* 60: 1038–47. <https://doi.org/10.1016/j.actamat.2011.10.061>.
- Thompson, M. S., Zega, T. J., Becerra, P., Keane, J. T., and Byrne, S. 2016. The Oxidation State of Nanophase Fe Particles in Lunar Soil: Implications for Space Weathering. *Meteoritics & Planetary Science* 51: 1082–95. <https://doi.org/10.1111/maps.12646>.
- Ulf-Møller, F. 1998. Effects of Liquid Immiscibility on Trace Element Fractionation in Magmatic Iron Meteorites: A Case Study of Group IIIAB. *Meteoritics & Planetary Science* 33: 207–220.
- Ulrich, G. E., Hodges, C. A., and Muehlberger, W. R. 1981. Geology of the Apollo 16 Area, Central Lunar Highlands. *United States Geological Survey Professional Papers* 1048: 548.
- Valley, J. W., Cavosie, A. J., Ushikubo, T., Reinhard, D. A., Lawrence, D. F., Larson, D. J., Clifton, P. H., et al. 2014. Hadean Age for a Post-Magma-Ocean Zircon Confirmed by Atom-Probe Tomography. *Nature Geoscience* 7: 219–223. <https://doi.org/10.1038/ngeo2075>.
- Walker, R. J. 2009. Highly Siderophile Elements in the Earth, Moon and Mars: Update and Implications for Planetary Accretion and Differentiation. *Chemie der Erde* 69: 101–125. <https://doi.org/10.1016/j.chemer.2008.10.001>.



- Walter, M. J., Newsome, H. E., Ertel, W., and Holzheid, A. 2000. Siderophile Elements in the Earth and Moon: Metal/Silicate Partitioning and Implications for Core Formation. In *Origin of the Earth and Moon*, edited by R. M. Canup, and K. Righers, 265–289. Tuscon, AZ: University of Arizona Press.
- Wasson, J. T., Chen-Lin, C., Robinson, K. L., and Baedecker, P. A. 1975. Siderophiles and Volatiles in Apollo-16 Rocks and Soils. *Geochimica et Cosmochimica Acta* 39: 1475–85. [https://doi.org/10.1016/0016-7037\(75\)90149-0](https://doi.org/10.1016/0016-7037(75)90149-0).
- Wasson, J. T., Huber, H., and Malvin, D. J. 2007. Formation of IIAB Iron Meteorites. *Geochimica et Cosmochimica Acta* 71: 760–781. <https://doi.org/10.1016/j.gca.2006.09.032>.
- Wasson, J. T., Ouyang, X., Wang, J., and Eric, J. 1989. Chemical Classification of Iron Meteorites: XI. Multi-Element Studies of 38 New Irons and the High Abundance of Ungrouped Irons from Antarctica. *Geochimica et Cosmochimica Acta* 53: 735–744. [https://doi.org/10.1016/0016-7037\(89\)90016-1](https://doi.org/10.1016/0016-7037(89)90016-1).
- Wiesli, R. a., Beard, B. L., Taylor, L. a., and Johnson, C. M. 2003. Space Weathering Processes on Airless Bodies: Fe Isotope Fractionation in the Lunar Regolith. *Earth and Planetary Science Letters* 216: 457–465. [https://doi.org/10.1016/S0012-821X\(03\)00552-1](https://doi.org/10.1016/S0012-821X(03)00552-1).
- Wood, B. J., Smythe, D. J., and Harrison, T. 2019. The Condensation Temperatures of the Elements: A Reappraisal. *American Mineralogist* 104: 844–856. <https://doi.org/10.2138/am-2019-6852CCBY>.
- Wszolek, P. C., Simoneit, B., and Burlingame, A. L. 1973. Studies of Magnetic Fines and Volatile-Rich Soils: Possible Meteoritic and Volcanic Contributions to Lunar Carbon and Light Element Chemistry. *Geochimica et Cosmochimica Acta* 2: 1693–1706.
- Xie, Z., Gopon, P., Xia, Y., Douglas, J. O., Cline, J., Liu, J., Tan, Q., et al. 2023. Does SW China Have Carlin-Type Gold Deposits? A Micro- and Atomic Scale Perspective. *Mineralium Deposita* 59: 757–772. <https://doi.org/10.1007/s00126-023-01231-6>.

## SUPPORTING INFORMATION

Additional supporting information may be found in the online version of this article.

**Supplementary A.** Data table with all EPMA and APT analyses conducted in this study.

**Supplementary B.** Combined sequential EDS/FIB-SEM sample preparation workflow for the preparation of APT samples that contain internal metallic particles.

**Supplementary C.** FIB-SEM lift-out locations for the APT analyses of the core and rim occurrences of

iron metal. Approximate locations of APT analyses are noted.

**Supplementary D.** APT reconstructions of the three successful data sets, with atom maps of Fe, Ni, and S/Si/Pt shown separately.

**Supplementary E.** Labeled APT mass spectrum of data set C1 (run # R5083\_7939).

**Supplementary F.** Labeled APT mass spectrum of data set R1 (run # R5083\_6622).

**Supplementary G.** Labeled APT mass spectrum of data set R2 (run # R5083\_6504).